

1 **Revision 1**

2 **Raman Spectroscopic Investigation of Selected Natural Uranyl Sulfate Minerals**

3 **Tyler L. Spano¹, Travis A. Olds², Marshall McDonnell³, Robert Smith³, and Ashley E.**
4 **Shields¹**

5 *¹Nuclear Nonproliferation Division, Oak Ridge National Laboratory, 1 Bethel Valley Road, Oak*
6 *Ridge, Tennessee, 37831, USA*

7 *²Carnegie Museum of Natural History, 4400 Forbes Avenue, Pittsburgh, Pennsylvania, 15213,*
8 *USA*

9 *³Computer Science and Mathematics Division, Oak Ridge National Laboratory, 1 Bethel Valley*
10 *Road, Oak Ridge, Tennessee, 37831, USA*

11 **Abstract**

12 Uranyl sulfates are important constituents of uranium ores and represent a significant fraction of
13 U(VI) minerals discovered in recent years owing to their propensity to form in mine tailings and
14 legacy sites related to uranium exploration. Recently, we surveyed all published Raman spectra
15 for uranium minerals and found significantly less easily accessible data available for uranyl
16 sulfates relative to other groups of uranium minerals. In that work we described average spectra
17 for groups of uranyl minerals to understand common vibrational spectroscopic features attributable
18 to similarities in oxyanion chemistry among U(VI) minerals, but only data for three uranyl sulfate
19 minerals were included in the study. The present work reports on Raman spectra collected for 18
20 additional uranyl sulfate minerals. To better understand underlying structural and chemical
21 features that give rise to spectroscopic observables, we relate differences in structural topology,
22 charge balancing cations, and locality of origin to features observed in the Raman spectra of
23 selected natural uranyl sulfates.

24 **Keywords:** uranyl sulfates, Raman spectroscopy, U(VI) minerals

This manuscript has been authored by UT-Battelle, LLC, under contract DE-AC05-00OR22725 with the US Department of Energy (DOE). The US government retains and the publisher, by accepting the article for publication, acknowledges that the US government retains a nonexclusive, paid-up, irrevocable, worldwide license to publish or reproduce the published form of this manuscript, or allow others to do so, for US government purposes. DOE will provide public access to these results of federally sponsored research in accordance with the DOE Public Access Plan (<http://energy.gov/downloads/doe-public-access-plan>)

25

Introduction

26 Accurate, nondestructive identification of uranium-bearing compounds is of critical
27 interest in the fields of nuclear forensics, environmental remediation, and resource exploration.

28 Uranyl sulfate minerals are important constituents of uranium ore deposits, occurring as
29 weathering products via oxidation-hydration alteration of primary uranium oxides such as
30 uraninite (Plášil, 2014). The propensity for uranyl sulfate occurrences are due in part to the
31 interaction of decomposing primary sulfide phases, resulting in low-pH, aqueous complexes of
32 UO_2^{2+} and SO_4^{2-} (Finch and Murakami, 1999; Krivovichev and Plášil, 2013). Analogously,
33 sulfuric acid is commonly employed during uranium extraction and milling operations (Seidel,
34 1981; Sharifironizi et al., 2016), resulting in a diverse population of technogenic uranyl sulfate
35 phases (Guettaf et al., 2009; Ling et al., 2010).

36 Systematic descriptions of both naturally occurring (Burns et al., 2003; Finch and
37 Murakami, 1999; Gurzhiy and Plášil, 2019; Krivovichev and Plášil, 2013; Tyumentseva et al.,
38 2019) and technogenic (Kohlgruber et al., 2022; Smith et al., 2018; Tyumentseva et al., 2019)
39 uranyl sulfates species are provided elsewhere. Briefly, uranyl sulfate minerals are composed of
40 U(VI) in pentagonal bipyramidal coordination, further linked through edge- and vertex-shared
41 SO_4 tetrahedra, forming a topologically diverse group of minerals. Currently, 46 uranyl sulfate
42 minerals are recognized by the International Mineralogical Association, making sulfates the most
43 numerous group of uranyl minerals. Linkages between U(VI) and S(VI) polyhedra are typically
44 monodentate with few exceptions (Burns et al., 2003; Gurzhiy and Plášil, 2019). Uranyl sulfate
45 minerals predominantly form sheet-like 2-D structures, however, some are known to crystallize
46 with infinite chain topologies, and few structures with isolated clusters of polyhedra are reported.
47 In addition to classification based upon structure type, uranyl sulfates may also be categorized by

48 relations between their overall bond topologies with previously described species (Burns, 2005;
49 Lussier et al., 2016). Gurzhiy and Plášil (Gurzhiy and Plášil, 2019) describe eight categories of
50 structural topologies in which uranyl sulfate minerals may be grouped, including the zippeite
51 (Burns et al., 2003), leydetite (Plášil et al., 2013b), phosphuranylite (Demartin et al., 1991), and
52 mathesiusite (Plášil et al., 2014c) topologies, as well as isolated clusters, chains of polyhedra,
53 dense chains of polyhedra, and rare layers (Gurzhiy and Plášil, 2019).

54 To elucidate the relationships between structural attributes and observable spectroscopic
55 features, here we discuss in detail the Raman spectra of uranyl sulfate minerals and the
56 underlying crystallographic features from which they originate. This work focuses on mineral
57 species possessing the zippeite, mathesiusite, and phosphuranylite anion topologies and members
58 of the uranyl sulfates that are composed of isolated clusters, chains of polyhedra, and dense
59 chains of polyhedra, as delineated by Gurzhiy and Plášil (Gurzhiy and Plášil, 2019). First,
60 common features are examined in the spectra of all uranyl sulfate minerals, then we discuss
61 average spectra calculated for groups of uranyl sulfate minerals based on structure type (and
62 anion topology). As a means towards understanding potential crystal–chemical influences that
63 charge balancing cations may have on observable spectroscopic features, we examine differences
64 between the spectra of individual mineral species belonging to a given structural group. Finally,
65 we explore the possible influence of sample origin (locality) on spectroscopic observations on
66 minerals of the same species.

67 **Materials and Methods**

68 Uranyl sulfate minerals investigated in this work are summarized in Table 1 and include
69 Co-rich zippeite (Burns et al., 2003), Zn-rich zippeite (Burns et al., 2003), ammoniozippeite
70 (Kampf et al., 2018b), natrozippeite (Burns et al., 2003), uranopilite (Burns, 2001),

71 ammoniomathesiusite (Kampf et al., 2019c), johannite (Donnay, 1955; Mereiter, 1982),
72 marécottite (Brugger et al., 2003; Burns et al., 2003), lussierite (Kampf et al., 2019b),
73 zincorietveldite (Kampf et al., 2023), navrotskyite (Miyawaki et al., 2019), fermiite (Kampf et
74 al., 2015b), belakovskiite (Kampf et al., 2014), plášilite (Kampf et al., 2015a), feynmanite
75 (Kampf et al., 2019a), bluelizardite (Plášil et al., 2014b), meisserite (Plášil et al., 2013a), and
76 rabejacite (Plášil et al., 2014a). Crystalline samples of each mineral listed in Table 1 were
77 extracted from matrix as aggregates of crystalline material with a tungsten fine-tipped needle
78 (0.6 μm). The size of the crystals varied from finely powdered ($< 1 \mu\text{m}$ crystallite size, e.g.
79 zippeites D and E) to macroscopically crystalline ($\sim 20 \mu\text{m}$ and larger) for the remaining phases.
80 In some instances, the extracted aggregates contained adhering gypsum or asphaltum matrix.
81 Care was taken to ensure that adhering or other associated phases did not interfere with the
82 measured data, and that the spectra presented are phase pure. For each uranyl sulfate mineral
83 species investigated in this work, Raman spectra were collected using a Renishaw InVia micro-
84 Raman spectrometer with a 785 nm excitation wavelength equipped with a 1200 lines/mm
85 diffraction grating, resulting in a resolution of $\sim 2.5\text{--}3.1 \text{ cm}^{-1}$ and an approximate power density
86 of 100 W/cm^2 based upon laser power (10 mW) and spot size ($\sim 1 \mu\text{m}^2$). Data were collected as
87 20 accumulations of 10 s of data in the range of $50\text{--}1250 \text{ cm}^{-1}$. Raw data were imported into
88 OriginPro (2021) for analysis. To facilitate comparing spectra for minerals with varying Raman
89 signal intensity, each data set was normalized by dividing each data point by the integrated total
90 counts over the spectral range of interest.

91 **Results and Discussion**

92 **Average Uranyl Sulfate Spectrum and Average Spectra Based on Structure Type**

93 To understand common spectral features among uranyl minerals and technogenic phases
94 with similar chemical compositions, we recently determined average spectra for groups of uranyl
95 minerals based on secondary oxyanion chemistry (e.g., structural components in addition to U
96 and O) to apply as features for machine learning applications (McDonnell et al., 2022; Spano et
97 al., 2023). In addition, we used principal component analyses combined with partial least squares
98 regression to reveal additional underlying chemical and structural features that could contribute
99 to optical vibrational spectroscopic observables and potentially lead to identification of unknown
100 U-rich materials. When calculating the average spectrum for uranyl sulfate minerals in that work,
101 we identified a lack of readily available Raman spectra for this group. Furthermore, the average
102 uranyl sulfate spectrum we reported notably lacked contributions from zippeite group minerals.
103 To better understand common characteristics of the Raman spectra of uranyl sulfates, the present
104 study details the new average spectrum for uranyl sulfate minerals, which contains the species
105 included in Table 1 in addition to the mineral spectra already included in CURIES (Compendium
106 of Uranium Raman and Infrared Experimental Spectra) (Spano et al., 2023). A comparison of the
107 previously published and new average spectra is shown in Figure 1.

108 The addition of new data sets to the average uranyl sulfate spectrum reveals several
109 notable features. At low energy, 3 bands of spectral intensity are observed, located at ~290, 321,
110 and 354 cm^{-1} . The features at ~290 and 354 cm^{-1} were present in the initial average spectrum but
111 are fully resolved in the updated average data set. A shoulder peak located at 396 cm^{-1} is now
112 visible in the updated average spectrum, coupled with an increase in intensity of the apparent
113 vibrational mode centered at 423 cm^{-1} . A diffuse, low-intensity band located at ~490 cm^{-1} in the
114 initial average spectrum is replaced by a broad apparent doublet of modes between 450 and 515
115 cm^{-1} in the updated version, attributable to $\nu_2 \text{SO}_4^{2-}$ bending in zippeite group species. Several

116 low intensity features are observed in the range of 590–680 cm^{-1} in the updated spectrum, likely
117 related to contributions from the $\nu_4 \text{SO}_4^{2-}$ bending vibrational mode present in zippeite group
118 uranyl sulfates. Most notably, the $\nu_1 \text{UO}_2^{2+}$ symmetric stretching vibrational mode, previously
119 centered at $\sim 837 \text{ cm}^{-1}$, is replaced by an apparent quartet of modes between 780–871 cm^{-1} ,
120 which corresponds to U-O_{y1} bond lengths between 1.83-1.74 Å based on the relationship between
121 bond length and $\nu_1 \text{UO}_2^{2+}$ frequency described by Bartlett and Cooney (1989). This additional
122 complexity is certainly attributable to the inclusion of spectra for more diverse uranyl sulfate
123 species with cluster, chain, and sheet structures now represented in the updated average uranyl
124 sulfate spectrum. 2 additional low-intensity bands centered at 916 and 936 cm^{-1} are visible in the
125 updated average spectrum. As was observed for the uranyl symmetric stretching vibrational
126 mode, an increase in relative intensity and complexity is seen in the SO_4^{2-} region of the updated
127 average spectra, with several low energy shoulders associated with an apparent triad of modes
128 between 985 and 1030 cm^{-1} attributable to symmetric and/or antisymmetric SO_4^{2-} stretching
129 vibrations. Although visible in the initial average spectrum for uranyl sulfates, the feature located
130 at $\sim 1045 \text{ cm}^{-1}$ is better resolved in the updated data. Finally, the broad peak centered at ~ 1093
131 cm^{-1} in the older data set is replaced by 2 spectral features centered at ~ 1075 and 1090 cm^{-1} ,
132 likely also related to SO_4^{2-} stretching vibrations (Frost et al., 2005a). These spectroscopic details
133 resulting from inclusion of additional uranyl sulfate spectra in CURIES will aid in determining
134 features associated with this oxyanion chemistry for machine learning applications.

135 Beyond investigating average uranyl sulfate mineral spectra for all species in this
136 oxyanion group, this study also determines the average spectra of groups of uranyl sulfates based
137 on their structure type. This information can provide insight into spectroscopic features imparted
138 by similarities in underlying structure or topology with a similar goal of using these features to

139 train machine learning models to recognize uranyl sulfates from Raman spectra. Figure 2 shows
140 average spectra calculated for members of the zippeite and phosphuranylite groups and average
141 spectra for uranyl sulfates composed of chains of polyhedra and isolated clusters, with details of
142 assignments provided in Table 2. Features of the uranyl region are discussed in detail elsewhere
143 (Lu et al., 2018), so this study focuses instead on interpretation of spectroscopic features that
144 originate from S–O and equatorial U–O (U-O_{eq}) vibrational modes.

145 The average spectrum of zippeite group sulfates is distinguished by a band centered at
146 157 cm^{-1} , an apparent quartet of modes between ~ 380 and 550 cm^{-1} , a doublet with a high-
147 energy shoulder in the uranyl region (~ 760 – 890 cm^{-1}), an apparent doublet of modes between
148 ~ 1000 and 1050 cm^{-1} , and a low-intensity peak centered at $\sim 1090\text{ cm}^{-1}$. The peak at 157 cm^{-1} ,
149 likely attributable to U-O_{eq} modes (Plášil et al., 2010) appears to be a unique feature of zippeite
150 group uranyl sulfates. Similarly, the spectral features observed between 380 and 550 cm^{-1} in the
151 average zippeite group spectrum appears to be signatory of this structure type relative to other
152 uranyl sulfates examined in this work, which are attributable to the overlap of $\nu_2\text{UO}_2^{2+}$, U-O_{eq} ,
153 and $\nu_3\text{SO}_4^{2-}$ modes of members of this group (discussed in the next section). Moving to the peak
154 centered at $1,015\text{ cm}^{-1}$ originating from the $\nu_1\text{SO}_4^{2-}$ symmetric stretching mode, we note that the
155 location of this vibration occurs at significantly higher energy ($\sim 15\text{ cm}^{-1}$ higher) relative to the
156 analogous mode in the average spectra of chains of polyhedra and isolated clusters. Likewise,
157 this is at lower energy than the appearance of the $\nu_1\text{SO}_4^{2-}$ in the average spectrum of
158 phosphuranylite group uranyl sulfates. Lower frequency $\nu_1\text{SO}_4^{2-}$ vibrations in the zippeite group
159 (relative to phosphuranylite species) may result from coordination effects—every sulfate group
160 in the zippeite topology shares vertices with a U coordination polyhedra, perhaps limiting the
161 extent of atomic motion.

162 The average spectrum for phosphuranylite group uranyl sulfates is characterized by low
163 intensity spectral features centered at $\sim 205, 245, 450, 625, 880,$ and 1145 cm^{-1} . Additionally, an
164 intermediate intensity band is located at $\sim 1045 \text{ cm}^{-1}$, and an apparent doublet of modes appears
165 between 1070 and 1115 cm^{-1} . The bands located at 205 and 245 cm^{-1} in the average
166 phosphuranylite spectrum are likely attributable to ν_2 U–O–U bending modes based on
167 assignments for feynmanite by Kampf et al. (2019a). Similarly, the weak bands at ~ 450 and 625
168 cm^{-1} may be attributable to doubly and triply degenerate ν_2 and ν_4 SO_4^{2-} bending modes,
169 respectively (Kampf et al., 2018a). Contributions from the ν_1 SO_4^{2-} symmetric stretching
170 vibration are observed at $\sim 1045 \text{ cm}^{-1}$, with an additional doublet of bands belonging to ν_3 SO_4^{2-}
171 vibrations present between 1075 and 1115 cm^{-1} . The higher energy appearance of the ν_1 and ν_3
172 SO_4^{2-} modes in the average Raman spectrum of phosphuranylite group uranyl sulfates may be
173 used to distinguish species of this group from zippeite-type structures, where these same bands
174 are present at ~ 1015 and 1040 cm^{-1} .

175 The low-energy region of the average spectrum calculated for uranyl sulfates possessing
176 structures based on chains of polyhedra (rietveldite, navrotskyite, fermiite, and meisserite) is
177 characterized by a medium-intensity band centered at 230 cm^{-1} and several regions of low-
178 intensity spectral features between $\sim 320, 410\text{--}475,$ and $585\text{--}675 \text{ cm}^{-1}$. A distinct band centered
179 at 230 cm^{-1} is attributable to ν_2 U–O–U based on assignments for fermiite (Kampf et al., 2015b).
180 The high-energy region ($\sim 900 \text{ cm}^{-1}$ and above) is the most complex for this average spectrum
181 relative to other groups of uranyl sulfate minerals. The complexity seems to originate largely
182 from contributions of the fermiite and meisserite spectra to the average, which may be
183 attributable to the large number of crystallographically distinct SO_4^{2-} groups (4) in these species
184 relative to other uranyl sulfates composed of chains of polyhedra.

185 The average spectrum for uranyl sulfate minerals containing isolated clusters is
186 characterized by several areas of diffuse, low-intensity bands in the regions of 150–250, 415–
187 475, and 600–660 cm^{-1} . An additional low-intensity feature is observed at $\sim 935 \text{ cm}^{-1}$ with an
188 apparent triplet of modes centered at 1000 cm^{-1} , which distinguishes the average spectrum of
189 isolated cluster-type species from other uranyl sulfates. Although the position of the 1000 cm^{-1}
190 triplet of modes is centered similarly to the ν_1 and $\nu_3 \text{ SO}_4^{2-}$ modes in the average spectrum
191 calculated for uranyl sulfates possessing chains of polyhedra, the feature at 1000 cm^{-1} in the
192 average spectrum for isolated cluster uranyl sulfates is significantly broader than the analogous
193 1-D chain spectral peak.

194 **Zippeite Group**

195 Individual Raman spectra collected for uranyl sulfate minerals belonging to the zippeite
196 group (Figure 3) are shown in Figures 4a–c. Although the crystallographic symmetry and
197 chemical composition of zippeite group minerals are highly variable, some exhibit extensive
198 solid solution and they all contain topologically identical sheet structures. Minerals belonging to
199 this group are characterized by infinite sheets of uranyl pentagonal bipyramids linked through
200 sharing of equatorial edges and vertices (Figure 3a). Each uranyl pentagonal bipyramid shares
201 vertices with two sulfate tetrahedra, serving to form the extended sheet topology with a
202 characteristic U:S ratio of 2:1. A notable feature present in the Raman spectra of zippeite group
203 minerals is variability in the position of the $\nu_1 \text{ UO}_2^{2+}$ symmetric stretching vibrational mode
204 (Plášil et al., 2010). Natrozippeite spectra are characterized by a mode centered at 840 cm^{-1} ,
205 whereas Zn-rich zippeite, Co-rich zippeite, and marécottite possess a lower energy uranyl peak,
206 centered at approximately 810 cm^{-1} (Figure 4b). A low-intensity peak is also observed around
207 810 cm^{-1} in some of the spectra collected for natrozippeite, which we initially hypothesized

208 could result from either an admixture or solid solution with other zippeite group phases.
209 However, Plášil et al. note that significant polarization dependence is possible when collecting
210 Raman spectra for zippeite. Resultingly, we believe this contribution originates a slight shift in
211 the position of $\nu_1 \text{UO}_2^{2+}$ arising from differences in the orientation of individual crystallites in the
212 sample we analyzed (Plášil et al., 2010) . Both ammoniozippeite and rabejacite spectra show
213 uranyl vibrational mode positions that are distinct from other zippeite group phases, with broad,
214 relatively low intensity vibrational modes centered at $\sim 831 \text{ cm}^{-1}$ for ammoniozippeite and 852
215 cm^{-1} for rabejacite (Figure 4b). Differences are also observed in the $\nu_1 \text{SO}_4^{2-}$ vibrational mode
216 amongst zippeite group species. Like observations of the $\nu_1 \text{UO}_2^{2+}$, Zn-rich zippeite, Co-rich
217 zippeite, and marécottite have similarly positioned $\nu_1 \text{SO}_4^{2-}$ modes, centered at approximately
218 1015 cm^{-1} however, despite the distinct uranyl band observed in ammoniozippeite, the $\nu_1 \text{SO}_4^{2-}$
219 symmetric sulfate stretching mode also appears here (Plášil et al., 2010). Natrozippeite spectra
220 show a lower energy $\nu_1 \text{SO}_4^{2-}$ centered at $\sim 1010 \text{ cm}^{-1}$. Likewise, the $\nu_1 \text{SO}_4^{2-}$ mode in rabejacite
221 is found at higher energy, $\sim 1035 \text{ cm}^{-1}$. The position of the $\nu_3 \text{SO}_4^{2-}$ mode is also variable in the
222 zippeite group. In general, the position of this mode is centered at $\sim 1090 \text{ cm}^{-1}$ in natrozippeite,
223 although additional spectral features are present at higher energy in some specimens examined,
224 which may obscure the appearance of this mode. The variability in the background of
225 natrozippeite spectra at high energy may be attributable to different host rock species for the
226 samples examined related to the varied localities from which they originate. Further differences
227 between natrozippeite spectra from different localities will be discussed in a later section. Zn-
228 rich zippeite, Co-rich zippeite, ammoniozippeite, and marécottite have similar spectral positions
229 for the $\nu_3 \text{SO}_4^{2-}$, with this mode appearing at $\sim 1095 \text{ cm}^{-1}$ and likely arising from structural
230 similarities between these zippeite species. The $\nu_3 \text{SO}_4^{2-}$ mode in rabejacite is found at higher

231 energy, centered at $\sim 1115\text{ cm}^{-1}$. Significant complexity is observed in the low-energy region of
232 zippeite group uranyl sulfate spectra.

233 In general for zippeite group species, the $\nu_1\text{ UO}_2^{2+}$ mode appears at approximately
234 275 cm^{-1} , equatorial (U-O_{eq}) modes at $\sim 350\text{--}375\text{ cm}^{-1}$, and $\nu_3\text{ SO}_4^{2-}$ modes at approximately
235 $\sim 400\text{--}500\text{ cm}^{-1}$, all based on assignments from Frost et al. (2005a). The low-energy region of
236 spectra collected for zippeite group uranyl sulfates is shown in Figure 4c. In general, spectral
237 features of Zn-rich zippeite coincide with low-wavenumber modes for Co-rich zippeite and
238 marécottite. Ammoniozippeite, natrozippeite, and rabejacite modes appear to be shifted relative
239 to these species. However, natrozippeite shows 2 bands of intermediate intensity at 191 and 396
240 cm^{-1} , ammoniozippeite has similar spectral features centered at 150 and 405 cm^{-1} , and in
241 rabejacite, these are found at 165 and 455 cm^{-1} . Although no assignments are available for
242 modes below 200 cm^{-1} from Frost et al., these authors assign modes between 400 and 500 cm^{-1}
243 to U–O equatorial vibrations. The observed spectral shifts in this region likely originate from a
244 combination of various lattice vibrations and differences in equatorial O bond strengths imparted
245 by interactions with different interstitial charge balancing cations.

246 **Phosphuranylite Group**

247 Johannite, plášilite, and feynmanite (Figure 5a) all contain sheets composed of dimers of
248 uranyl pentagonal bipyramids interlinked through sharing of vertices with uranyl sulfate
249 tetrahedra (Figure 5b). Structural differences between these species arise from changes in the
250 manner in which uranyl pentagonal dimeric units are interlinked via sulfate tetrahedra and, in
251 particular, the direction in which apical O associated with SO_4^{2-} tetrahedra are pointing. These
252 distinct local directionalities are manifested in unique uranyl and sulfate vibrational mode
253 frequencies within the Raman spectra of these species (see Figure 6). Variations in the position

254 of the ν_1 UO_2^{2+} mode are observed in the spectra of these species, with peaks centered at ~ 830 ,
255 845, and 875 cm^{-1} for johannite, plášilite, and feynmanite, respectively (Frankland et al., 2022).
256 In general, SO_4^{2-} modes are also distinct when comparing the spectra of these species. Kampf et
257 al. (2019a) assign vibrational modes at 1075, 1042 and 1006 cm^{-1} in feynmanite to ν_1 SO_4^{2-}
258 symmetric stretching modes, and similarly, spectral intensities are observed at 1097, 1063, and
259 1029 cm^{-1} in our data for this species. The ν_1 SO_4^{2-} modes are observed in plášilite at slightly
260 lower energy than those for feynmanite, with peaks observed at ~ 1080 , 1045, and 1007 cm^{-1} . In
261 johannite, ν_1 and ν_3 SO_4^{2-} modes are seen at higher energy relative to feynmanite, with bands
262 centered at 1148 and 1045 cm^{-1} , respectively (Frankland et al., 2022; Frost et al., 2005b). A
263 doublet of modes is visible between 1070 and 1115 cm^{-1} in spectra collected for johannite and
264 appears to replace the medium-intensity vibrations observed at 1063 cm^{-1} in plášilite and 1045
265 cm^{-1} in feynmanite. These features may originate from lower space group symmetry in johannite
266 ($P-1$) relative to plášilite ($P2_1/c$) and feynmanite ($P2/n$). Significant background signal is
267 observed for plášilite and feynmanite, particularly in the low-energy region. It is unclear if this
268 signal indeed originates from these mineral species themselves (e.g., fluorescence) or from
269 matrix material with which they are associated, although optical examination (Figure 5a)
270 suggests that these are pure samples making fluorescence the more likely source of the additional
271 background signal.

272 Below 700 cm^{-1} , spectral complexity is limited for these mineral species. Johannite,
273 plášilite, and feynmanite spectra show bands around 200 cm^{-1} that are attributable to ν_2 O–U–O
274 bending modes (Frost et al., 2005b). The multiplicity of features here likely relates to both the
275 number of symmetrically unique O atoms that coordinate U centers and local symmetry
276 constraints of these sites. Between 350 and 400 cm^{-1} , low-intensity modes are observed in the

277 spectra of these 3 species. Based on assignments from Kampf et al. (2019a) for feynmanite, these
278 modes may originate from either U–O equatorial modes or O–M interactions, where M is the
279 charge balancing interstitial species. A few low-intensity peaks are observed between 400 and
280 700 cm^{-1} for johannite, plášilite, and feynmanite, which are assigned to $\nu_4 \text{SO}_4^{2-}$ ($\sim 450\text{--}490$
281 cm^{-1}) and $\nu_2 \text{SO}_4^{2-}$ ($\sim 610\text{--}650 \text{cm}^{-1}$).

282 **Chains of Polyhedra**

283 Fermiite, meisserite, navrotskyite, and Zn-rich rietveldite (Figure 7a) all contain chains of
284 uranyl pentagonal bipyramidal polyhedra interlinked through sharing of vertices with either four
285 or five SO_4^{2-} tetrahedral units (Figure 7b). Although diversity exists in the position of the ν_1
286 UO_2^{2+} mode in spectra for minerals in this group (Figure 8), a few common features are observed
287 between 400 and 700 cm^{-1} . First, spectra for fermiite, navrotskyite, meisserite, and rietveldite all
288 show low-intensity bands between 405 and 480 cm^{-1} , which, based on assignments from Kampf
289 et al. and Plášil et al. (Kampf et al., 2015b; Kampf et al., 2017; Plášil et al., 2013a), can be
290 attributed to $\nu_2 \text{SO}_4^{2-}$ bending modes. Similarly, all species show low-intensity spectral features
291 between ~ 580 and 675 cm^{-1} , which are assigned as $\nu_4 \text{SO}_4^{2-}$ modes. Significant variability in the
292 position of the $\nu_1 \text{UO}_2^{2+}$ mode is observed, with intensities centered at 824, 847, and 856 cm^{-1}
293 for fermiite, meisserite, and rietveldite, respectively. Two spectra of navrotskyite were collected,
294 and there appears to be variability in the position of the uranyl peak for the 2 data sets, with
295 modes observed at 846 and 850 cm^{-1} for data collected on 2 individual crystals of the same
296 sample. Differences in the SO_4^{2-} region are also observed between the two crystals of the
297 navrotskyite sample we examined. One shows a doublet of modes with a higher-intensity feature
298 centered at 1000 cm^{-1} and a lower-intensity peak at 982 cm^{-1} . The other crystal spectrum shows
299 a triplet of modes with 2 low-intensity peaks at 982 and 1000 cm^{-1} and a more intense peak at

300 1013 cm^{-1} . One of the samples of navrotskyite shows similarity to spectra collected for fermiite.
301 However, optical images of the navrotskyite sample suggest that no additional phases are present
302 (Figure 7a) and may indicate that this phase can either form a solid solution series, be intergrown
303 with a similar, but distinct, mineral species, or possess polarization dependence similar to
304 zippeite group minerals. Additional investigations beyond the scope of this work may prove
305 useful towards determining the origin of spectral signatures we observe for navrotskyite. Of all
306 the uranyl species composed of chains of polyhedra, the sulfate region of fermiite is the most
307 complex with multiple well-resolved bands located between 900 and 1200 cm^{-1} . Although this
308 complexity may originate from four crystallographically distinct S atoms in fermiite, meisserite
309 also possess four unique S sites, and the spectra for this phase are simpler in the sulfate region
310 relative to fermiite. However, comparison of the number of crystallographically unique O sites in
311 fermiite (33) with meisserite (19), suggests that variability in O is the more likely origin of the
312 additional peaks in the 900 to 1200 cm^{-1} region of the spectrum. Of the modes observed in
313 fermiite, 2 are at higher energy relative to other sulfate modes in this group of minerals with
314 peaks seen at ~ 1070 and 1185 cm^{-1} originating from triply degenerate $\nu_3 \text{SO}_4^{2-}$ vibrations
315 (Kampf et al., 2015b). Meisserite spectra show significant broadening and background
316 contributions below 900 cm^{-1} , perhaps originating from fluorescence of this phase.

317 **Isolated Clusters**

318 Belakovskiite, lussierite, and bluelizardite (Figure 9a) are comprised of isolated clusters
319 of uranyl pentagonal bipyramidal polyhedra further coordinated by either four or five sulfate
320 tetrahedra (Figure 9b) and, qualitatively, have greater structural differences between them than
321 other groups of uranyl sulfate minerals discussed in this study so far. Belakovskiite possesses
322 four crystallographically distinct monodentate sulfate tetrahedra bonded to a pentagonal

323 bipyramidally coordinated U center, and an additional sulfate tetrahedra linked only to Na and
324 H₂O. The fifth equatorial O atom coordinating U in this species is an H₂O group (Kampf et al.,
325 2014). Lussierite, also containing U in pentagonal bipyramidal geometry, possesses bidentate
326 coordination in the form of an edge-sharing sulfate group and three additional monodentate
327 sulfate tetrahedra coordinating the U center (Kampf et al., 2019b). The structural unit of
328 blue lizardite is characterized by dimers of uranyl pentagonal bipyramids interconnected by two
329 shared sulfate tetrahedra (Plášil et al., 2014b). Each uranyl center is further coordinated by three
330 additional sulfate groups to form isolated clusters (Figure 9b). These structural differences are
331 manifested in the Raman spectra of these phases (Figure 10). Although the ν_1 UO₂²⁺ modes of
332 blue lizardite and belakovskiite appear in similar positions at ~ 845 cm⁻¹, a significant redshift is
333 observed for the same mode in the spectra of lussierite. The lower energy of the uranyl mode in
334 lussierite is perhaps attributable to weaker U–O_{yl} bond strengths related to the presence of an
335 edge-sharing (rather than vertex sharing) sulfate group. Indeed, bond valence sums provided by
336 Kampf et al. (2019b) indicate that U in lussierite is slightly overbonded (6.10 valence units [vu])
337 with respect to blue lizardite (5.98 vu) (Plášil et al., 2014b). However, more pronounced
338 overbonding is observed for U in belakovskiite (6.22 vu) (Kampf et al., 2014) relative to other
339 uranyl sulfates with structures composed of isolated clusters, suggesting that overbonding is not
340 the origin of the lower energy uranyl signal in lussierite relative to other uranyl sulfates
341 composed of isolated clusters.

342 The sulfate regions of belakovskiite, lussierite, and blue lizardite spectra are complex and
343 highlight the structural information that is extractable from spectroscopic data. In belakovskiite,
344 an intense peak is observed at ~ 1010 cm⁻¹, with medium- and low-intensity shoulder modes
345 observed at ~ 980 and 1050 cm⁻¹, respectively. Similarly, an apparent triplet of modes is seen

346 between 970 and 1040 cm^{-1} in bluelizardite. Far more complicated is the region between 920 and
347 1090 cm^{-1} in the spectrum of lussierite, which possesses the largest number (6) (Kampf et al.,
348 2019b) of crystallographically distinct sulfate groups relative to bluelizardite (4) (Plášil et al.,
349 2014b) and belakovskiite (5) (Kampf et al., 2014). Peaks in this region originate from ν_1 and ν_3
350 SO_4^{2-} modes (Plášil et al., 2014b). The unique equatorial linkages in lussierite and belakovskiite
351 are also reflected in the low-energy regions of the Raman spectra. Only one band is seen for
352 bluelizardite at $\sim 200 \text{ cm}^{-1}$ and is assigned to $\nu_2 \text{UO}_2^{2+}$, 2 modes are observed for belakovskiite
353 and lussierite, with the latter displaying an additional low-energy peak at $\sim 124 \text{ cm}^{-1}$. Similarly, 1
354 $\nu_2 \text{SO}_4^{2-}$ (450 cm^{-1}) mode is observed for bluelizardite, whereas additional modes are seen for
355 other species in this region. Likewise, additional $\nu_4 \text{SO}_4^{2-}$ ($\sim 630 \text{ cm}^{-1}$) modes are observed for
356 belakovskiite and lussierite relative to bluelizardite.

357 **Other Uranyl Sulfates: Uranopilite and Ammoniomathesiusite**

358 In addition to uranyl sulfates categorized as belonging to the zippeite or phosphuranylite
359 groups or possessing structures based on chains of polyhedra or isolated clusters, this study also
360 investigates two uranyl sulfate minerals that do not belong to any of those categories. Uranopilite
361 contains dense chains of polyhedra (Burns, 2001; Colmenero et al., 2020), whereas
362 ammoniomathesiusite is a uranyl sulfate vanadate (Kampf et al., 2019c). To investigate unique
363 features in the Raman spectra of these phases, we have compared the Raman spectra for
364 uranopilite and ammoniomathesiusite to average spectra calculated for groups of uranyl sulfate
365 minerals discussed in previous sections.

366 When comparing the Raman spectrum of uranopilite to those of other groups of uranyl
367 sulfate minerals (see Supporting Information, Figure S1), a higher energy $\nu_1 \text{UO}_2^{2+}$ centered at
368 863 cm^{-1} is observed. A unique band centered at 567 cm^{-1} is also seen, which readily

369 distinguishes uranopilite from any other uranyl sulfate phase. The difference is visible because
370 no mode is seen at this frequency in the average spectra of uranyl sulfates belonging to the
371 zippeite group, nor is this mode seen in the average spectra of uranyl sulfates possessing chains
372 of polyhedra or isolated clusters. Based on assignments provided by Frost et al., the band
373 centered at 567 cm^{-1} originates from either ν_2 or ν_4 SO_4^{2-} bending vibrations. If this mode is
374 indeed a ν_2 , it occurs at significantly higher energy than the same mode in other uranyl
375 phosphates with structures possessing chains of polyhedra. Likewise, if this mode is a ν_4 , it is
376 found at significantly lower energy than the same mode in the average spectra of uranyl sulfates
377 with chains of polyhedra. Colmenero et al.(2020) provide a detailed computational investigation
378 of the infrared (IR) spectra of uranopilite using density functional perturbation theory and note
379 several modes in the range of $400\text{-}600\text{ cm}^{-1}$. Unfortunately, we cannot assign our experimental
380 Raman spectra from these computational results without the character of the predicted modes,
381 and thus the ability to discern between Raman and/ or IR active modes. Additional future
382 computational studies may provide clarity as to the identity of this mode.

383 Ammoniomathesiusite possesses square pyramidal vanadyl units in addition to uranyl and
384 sulfate coordination polyhedra. Resultingly, the spectrum of this mineral is distinct from any
385 other group of uranyl sulfate minerals (see Supporting Information, Figure S2). The ν_1 UO_2^{2+}
386 mode is centered at 836 cm^{-1} and cannot be used as a diagnostic spectral feature of this phase
387 because this is a similar position observed in other uranyl sulfates. However, 2 higher-energy
388 modes located at ~ 980 and $\sim 1010\text{ cm}^{-1}$, attributable to ν_1 V–O and S–O modes, respectively, are
389 unique to ammoniomathesiusite relative to uranyl sulfates with other structure types (Kampf et
390 al., 2019c).

391 **Locality Differences: Uranopilite**

392 Frost et al. investigated several samples of uranopilite from varying origins to gain
393 insight into molecular structure variability that may arise from different geochemical settings
394 (Frost et al., 2007). We take a similar approach and compare two data sets for uranopilite and
395 three data sets for natrozippeite from different localities. Spectra for two samples of uranopilite
396 are shown in Figure 11. Data collected for the sample from Apex mine were obtained from
397 RRUFF (Lafuente B, 2015) and were collected with a 780 nm excitation wavelength, whereas
398 the sample from Burro mine studied here was analyzed using a 785 nm laser. Qualitatively, we
399 observe good agreement between the 2 spectra, although data collected with the 780 nm laser
400 appear slightly redshifted compared to our 785 nm data. The ν_1 uranyl peak, located at 843 cm^{-1}
401 in the Burro sample, is found at 839 cm^{-1} in the Apex sample. Both spectra appear to possess a
402 shoulder associated with the uranyl band, which may be attributable to slight differences in local
403 coordination environments amongst the six symmetrically distinct U sites (Colmenero et al.,
404 2020). Frost et al. pose that owing to symmetry lowering of the uranyl unit, all uranyl and sulfate
405 vibrational modes are active in both Raman and infrared spectra (Frost et al., 2007). However,
406 we see no such evidence. When bending of the linear axial O–U–O occurs, it is possible that the
407 symmetry-forbidden $\nu_3\text{ UO}_2^{2+}$ mode appears at $\sim 900\text{ cm}^{-1}$ in the Raman resulting from a
408 breakdown of selection rules. However, no peaks are observed in this region for both uranopilite
409 data sets. Slight differences between the position of the $\nu_1\text{ SO}_4^{2-}$ symmetric stretching mode are
410 also observed for the 2 samples, with peaks centered at ~ 1010 and 1005 cm^{-1} for the Burro and
411 Apex samples, respectively. An apparent triplet of modes is observed at 1097, 1118, and 1145
412 cm^{-1} in the Burro sample, corresponding to the triply degenerate $\nu_3\text{ SO}_4^{2-}$. Similar features are
413 observed in the spectrum of uranopilite from the Apex mine; however, we provide slightly
414 higher spectral resolution in the data set from Burro. Low-energy modes in the spectra of

415 uranopilite from both samples are in good agreement, but the Burro sample possesses lower
416 background signal, which enables better definition of vibrational modes below 700 cm^{-1} .

417 **Locality Differences: Natrozippeite**

418 Slight differences in spectra for natrozippeite are observed when comparing data sets
419 from different localities (Figure 12). Unlike uranopilite, the $\nu_1\text{ UO}_2^{2+}$ vibrational mode in
420 natrozippeite samples is consistent and appears at 840 cm^{-1} regardless of the locality. All spectra
421 show a low-energy shoulder associated with the uranyl band at $\sim 813\text{ cm}^{-1}$; however, the
422 spectrum collected for the natrozippeite from the Markey mine appears to have a third low-
423 intensity band located between the 2 uranyl modes at $\sim 825\text{ cm}^{-1}$ (Figure 12a, inset). This
424 difference suggests that additional structural intricacy in the form of an intermediate U–O_{y1} bond
425 distance is present in this sample (Bartlett and Cooney, 1989; Frost et al., 2005a). At 1010 cm^{-1}
426 for all natrozippeite samples, the $\nu_1\text{ SO}_4^{2-}$ symmetric stretching mode is observed. The Blue
427 Lizard and Burro mine natrozippeite appear to have a low-intensity shoulder centered at ~ 1000
428 cm^{-1} , whereas the Markey mine spectrum shows an additional band at much lower energy, ~ 975
429 cm^{-1} . This result again suggests that slight structural distortions are present, potentially
430 attributable to variations in locality, and thus, specific geochemical conditions leading to
431 natrozippeite formation (e.g. pH, evaporation rate, etc.). Bands associated with $\nu_3\text{ SO}_4^{2-}$
432 vibrations are observed at ~ 1080 and 1090 cm^{-1} for all 3 natrozippeite samples. However, there
433 appears to be some qualitative differences in the line shape of the $\nu_3\text{ SO}_4^{2-}$ bands, which could
434 indicate differences in the static vs. dynamic polarizability of this mode, although the exact
435 origin of these differences is unclear at this time. We also observe a broad band at $\sim 1186\text{ cm}^{-1}$ in
436 the Markey mine sample that is not seen in natrozippeite spectra from other localities.
437 Differences in mineral habit are also observed when comparing three samples of natrozippeite

438 (Figure 12b). The Blue Lizard specimen displays euhedral platy aggregates, and the Markey
439 sample is powdery and cryptocrystalline. Natrozippeite from Burro mine has a somewhat
440 intermediate appearance relative to the other specimens, with small but visible crystallites
441 forming massive aggregates.

442 **Conclusions**

443 We have collected Raman spectra for 18 uranyl sulfate minerals after identifying an
444 absence in readily available spectra for these phases. To build a fundamental understanding of
445 common spectral features that relate to uranyl sulfate crystal structures, we present an updated
446 average uranyl sulfate Raman spectrum and suggest potential structural contributions to observed
447 vibrational modes. This study also describes average spectra of groups of uranyl minerals based
448 on structure type. Comparison of spectra within groups of uranyl sulfate minerals based on
449 structure type has also provided insight into the structural origins of observed spectral features,
450 including six members of the zippeite group (including four varieties of natrozippeite), three
451 species with the phosphuranylite anion topology, four minerals composed of chains of polyhedra,
452 three species with structure based on isolated clusters, and two additional uranyl sulfate phases
453 that do not fit into these categories. We have also compared spectra of uranopilite and
454 natrozippeite from different mines and discuss differences therein that could be attributable to
455 their localities of origin.

456 **Implications**

457 In the United States and internationally, legacy radionuclide contamination produced
458 during certain stages of the nuclear fuel cycle has had a lasting effect on the environment and
459 will continue to do so for thousands of years. For example, abandoned uranium mines and tailing

482 This work was partially funded by the Department of Energy's Oak Ridge National
483 Laboratory LDRD (Laboratory Directed Research and Development) program and the
484 Department of Energy's National Nuclear Security Administration Office of Defense Nuclear
485 Nonproliferation Research and Development. The authors sincerely thank Drs. Toya Beiswenger
486 and Jennifer Neu for their helpful comments and discussions regarding this work. Crystal
487 structure images were created using CrystalMaker.

488 **References**

- 489 (2021) OriginPro Version2021. OriginLab Corporation, Northampton, MA, USA.
- 490 Bartlett, J.R., and Cooney, R.P. (1989) On the determination of uranium-oxygen bond lengths in
491 dioxouranium (VI) compounds by Raman spectroscopy. *Journal of Molecular Structure*,
492 193, 295-300.
- 493 Brugger, J., Burns, P.C., and Meisser, N. (2003) Contribution to the mineralogy of acid drainage
494 of Uranium minerals: Marecottite and the zippeite-group. *American Mineralogist*, 88(4),
495 676-685.
- 496 Burns, P.C. (2001) A new uranyl sulfate chain in the structure of uranopilite. *The Canadian*
497 *Mineralogist*, 39(4), 1139-1146.
- 498 -. (2005) U⁶⁺ minerals and inorganic compounds: insights into an expanded structural hierarchy
499 of crystal structures. *The Canadian Mineralogist*, 43(6), 1839-1894.
- 500 Burns, P.C., Deely, K.M., and Hayden, L.A. (2003) The crystal chemistry of the zippeite group.
501 *The Canadian Mineralogist*, 41(3), 687-706.
- 502 Colmenero, F., Plášil, J., Timón, V., and Čejka, J. (2020) Full crystal structure, hydrogen
503 bonding and spectroscopic, mechanical and thermodynamic properties of mineral
504 uranopilite. *RSC Advances*, 10(53), 31947-31960.
- 505 Demartin, F., Diella, V., Donzelli, S., Gramaccioli, C., and Pilati, T. (1991) The importance of
506 accurate crystal structure determination of uranium minerals. I. Phosphuranylite
507 $\text{KCa}(\text{H}_3\text{O})_3(\text{UO}_2)_7(\text{PO}_4)_4\text{O}_4 \cdot 8\text{H}_2\text{O}$. *Acta Crystallographica Section B: Structural Science*,
508 47(4), 439-446.
- 509 Donnay, J. (1955) The primitive cell of johannite. *Mineralogical Society of America News and*
510 *Notes*.
- 511 Finch, R., and Murakami, T. (1999) Systematics and paragenesis of uranium minerals. In P.C.
512 Burns, and R. Finch, Eds. *Uranium: Mineralogy, Geochemistry and the Environment* 38.
513 Mineralogical Society of America.
- 514 Frankland, V.L., Milodowski, A.E., and Read, D. (2022) Laser-based characterisation of the
515 copper uranyl sulphate, johannite. *Minerals*, 12(11), 1419.
- 516 Frondel, C. (1958) *Systematic mineralogy of uranium and thorium*. US Government Printing
517 Office.

- 518 Frost, R., Weier, M., Bostrom, T., Čejka, J., and Martens, W. (2005a) Molecular structure of the
519 uranyl mineral zippeite-An XRD, SEM and Raman spectroscopic study. *Neues Jahrbuch*
520 *fur Mineralogie, Abhandlungen*, 181(3), 271-279.
- 521 Frost, R.L., Čejka, J., Weier, M.L., Martens, W.N., and Ayoko, G.A. (2007) Raman
522 spectroscopy of uranopilite of different origins—implications for molecular structure.
523 *Journal of Raman Spectroscopy*, 38(4), 398-409.
- 524 Frost, R.L., Erickson, K.L., Čejka, J., and Reddy, B.J. (2005b) A Raman spectroscopic study of
525 the uranyl sulphate mineral johannite. *Spectrochimica Acta Part A: Molecular and*
526 *Biomolecular Spectroscopy*, 61(11-12), 2702-2707.
- 527 Guettaf, H., Becis, A., Ferhat, K., Hanou, K., Bouchiha, D., Yakoubi, K., and Ferrad, F. (2009)
528 Concentration–purification of uranium from an acid leaching solution. *Physics Procedia*,
529 2(3), 765-771.
- 530 Gurzhiy, V.V., and Plášil, J. (2019) Structural complexity of natural uranyl sulfates. *Acta*
531 *Crystallographica Section B: Structural Science, Crystal Engineering and Materials*,
532 75(1), 39-48.
- 533 Kampf, A., Plášil, J., Kasatkin, A., and Marty, J. (2014) Belakovskiiite,
534 $\text{Na}_7(\text{UO}_2)(\text{SO}_4)_4(\text{SO}_3\text{OH})(\text{H}_2\text{O})_3$, a new uranyl sulfate mineral from the Blue Lizard
535 mine, San Juan County, Utah, USA. *Mineralogical Magazine*, 78(3), 639-649.
- 536 Kampf, A.R., Kasatkin, A.V., Čejka, J., and Marty, J. (2015a) Plášilite,
537 $\text{Na}(\text{UO}_2)(\text{SO}_4)(\text{OH})\cdot 2\text{H}_2\text{O}$, a new uranyl sulfate mineral from the Blue Lizard mine, San
538 Juan County, Utah, USA. *Journal of Geosciences*, 60(1), 1-10.
- 539 Kampf, A.R., Olds, T.A., Plášil, J., and Marty, J. (2023) Zincorietveldite,
540 $\text{Zn}(\text{UO}_2)(\text{SO}_4)_2(\text{H}_2\text{O})_5$, the zinc analogue of rietveldite from the Blue Lizard mine, San
541 Juan County, Utah, USA. *Mineralogical Magazine*, 1-22.
- 542 Kampf, A.R., Olds, T.A., Plášil, J., Marty, J., and Perry, S.N. (2019a) Feynmanite, a new sodium
543 uranyl sulfate mineral from Red Canyon, San Juan County, Utah, USA. *Mineralogical*
544 *Magazine*, 83(2), 153-160.
- 545 Kampf, A.R., Olds, T.A., Plášil, J., Nash, B.P., and Marty, J. (2019b) Lussierite, a new sodium
546 uranyl sulfate mineral with bidentate $\text{UO}_7\text{--SO}_4$ linkage from the Blue Lizard mine, San
547 Juan County, Utah, USA. *Mineralogical Magazine*, 83(6), 799-808.
- 548 Kampf, A.R., Plášil, J., Kasatkin, A.V., Marty, J., and Čejka, J. (2015b) Fermiite,
549 $\text{Na}_4(\text{UO}_2)(\text{SO}_4)_3\cdot 3\text{H}_2\text{O}$ and oppenheimerite, $\text{Na}_2(\text{UO}_2)(\text{SO}_4)_2\cdot 3\text{H}_2\text{O}$, two new uranyl
550 sulfate minerals from the Blue Lizard mine, San Juan County, Utah, USA. *Mineralogical*
551 *Magazine*, 79(5), 1123-1142.
- 552 Kampf, A.R., Plášil, J., Nash, B.P., and Marty, J. (2018a) Greenlizardite, $(\text{NH}_4)\text{Na}(\text{UO}_2)_2$
553 $(\text{SO}_4)_2(\text{OH})_2\cdot 4\text{H}_2\text{O}$, a new mineral with phosphuranylite-type uranyl sulfate sheets
554 from Red Canyon, San Juan County, Utah, USA ANTHONY R. KAMPF ET AL.
555 GREENLIZARDITE, NEW URANYL SULFATE FROM RED CANYON, UTAH.
556 *Mineralogical Magazine*, 82(2), 401-411.
- 557 -. (2019c) Ammoniomathesiusite, a new uranyl sulfate–vanadate mineral from the Burro mine,
558 San Miguel County, Colorado, USA. *Mineralogical Magazine*, 83(1), 115-121.
- 559 Kampf, A.R., Plášil, J., Olds, T.A., Nash, B.P., and Marty, J. (2018b) Ammoniozippeite, a new
560 uranyl sulfate mineral from the Blue Lizard Mine, San Juan County, Utah, and the Burro
561 Mine, San Miguel County, Colorado, USA. *The Canadian Mineralogist*, 56(3), 235-245.
- 562 Kampf, A.R., Sejkora, J., Witzke, T., Plášil, J., Čejka, J., Nash, B.P., and Marty, J. (2017)
563 Rietveldite, $\text{Fe}(\text{UO}_2)(\text{SO}_4)_2(\text{H}_2\text{O})_5$, a new uranyl sulfate mineral from Giveaway-Simplot

mine (Utah, USA), Willi Agatz mine (Saxony, Germany) and Jachymov (Czech Republic). *Journal of Geosciences*, 62(2), 107-120.

Kohlgruber, T.A., Perry, S.N., Sigmon, G.E., Oliver, A.G., and Burns, P.C. (2022) Hydrogen bond network and bond valence analysis on uranyl sulfate compounds with organic-based interstitial cations. *Journal of Solid State Chemistry*, 307, 122871.

Krivovichev, S.V., and Plášil, J. (2013) Mineralogy and crystallography of uranium. 15-119 p.

Lafuente B, D.R.T., Yang H, Stone N. (2015) The power of databases: the RRUFF project. *Highlights in Mineralogical Crystallography*, p. 1-30. De Gruyter.

Ling, J., Sigmon, G.E., Ward, M., Roback, N., and Burns, P.C. (2010) Syntheses, structures, and IR spectroscopic characterization of new uranyl sulfate/selenate 1D-chain, 2D-sheet and 3D-framework. *Zeitschrift für Kristallographie-Crystalline Materials*, 225(6), 230-239.

Lu, G., Haes, A.J., and Forbes, T.Z. (2018) Detection and identification of solids, surfaces, and solutions of uranium using vibrational spectroscopy. *Coordination chemistry reviews*, 374, 314-344.

Lussier, A.J., Lopez, R.A., and Burns, P.C. (2016) A revised and expanded structure hierarchy of natural and synthetic hexavalent uranium compounds. *The Canadian Mineralogist*, 54(1), 177-283.

McDonnell, M., Smith, R., Drane, L., Shields, A., Spano, T., Niedziela, J., Miskowiec, A., and Gibbs, I. (2022) Smart Spectral Matching (SSM). Oak Ridge National Lab.(ORNL), Oak Ridge, TN (United States).

Mereiter, K. (1982) The crystal structure of johannite, $\text{Cu}(\text{UO}_2)_2(\text{OH})_2(\text{SO}_4)_2 \cdot 8\text{H}_2\text{O}$. *Tschermaks Mineralogische und Petrographische Mitteilungen*, 30, 47-57.

Miyawaki, R., Hatert, F., Pasero, M., and Mills, S.J. (2019) New Minerals, Nomenclature and Classification (CNMNC), Newsletter 50. New minerals and nomenclature modifications approved in 2019. *Mineralogical Magazine*, 83.

Plášil, J. (2014) Oxidation-hydration weathering of uraninite: the current state-of-knowledge. *Journal of Geosciences*, 59(2), 99-114.

Plášil, J., Buixaderas, E., Čejka, J., Sejkora, J., Jehlička, J., and Novák, M. (2010) Raman spectroscopic study of the uranyl sulphate mineral zippeite: low wavenumber and U–O stretching regions. *Analytical and bioanalytical chemistry*, 397(7), 2703-2715.

Plášil, J., Dušek, M., Čejka, J., and Sejkora, J. (2014a) The crystal structure of rabejacite, the Ca^{2+} -dominant member of the zippeite group. *Mineralogical Magazine*, 78(5), 1249-1264.

Plášil, J., Kampf, A., Kasatkin, A., Marty, J., Škoda, R., Silva, S., and Čejka, J. (2013a) Meisserite, $\text{Na}_5(\text{UO}_2)(\text{SO}_4)_3(\text{SO}_3\text{OH})(\text{H}_2\text{O})$, a new uranyl sulfate mineral from the Blue Lizard mine, San Juan County, Utah, USA. *Mineralogical Magazine*, 77(7), 2975-2988.

Plášil, J., Kampf, A.R., Kasatkin, A.V., and Marty, J. (2014b) Bluelizardite, $\text{Na}_7(\text{UO}_2)(\text{SO}_4)_4\text{Cl}(\text{H}_2\text{O})_2$, a new uranyl sulfate mineral from the Blue Lizard mine, San Juan County, Utah, USA. *Journal of Geosciences*, 59(2), 145-158.

Plášil, J., Kasatkin, A., Škoda, R., Novák, M., Kallistová, A., Dušek, M., Skála, R., Fejfarová, K., Čejka, J., and Meisser, N. (2013b) Leydetite, $\text{Fe}(\text{UO}_2)(\text{SO}_4)_2(\text{H}_2\text{O})_{11}$, a new uranyl sulfate mineral from Mas d'Alary, Lodève, France. *Mineralogical Magazine*, 77(4), 429-441.

Plášil, J., Veselovský, F., Hloušek, J., Škoda, R., Novák, M., Sejkora, J., Čejka, J., Škácha, P., and Kasatkin, A.V. (2014c) Mathesiusite, $\text{K}_5(\text{UO}_2)_4(\text{SO}_4)_4(\text{VO}_5)(\text{H}_2\text{O})_4$, a new uranyl

609 vanadate-sulfate from Jáchymov, Czech Republic. *American Mineralogist*, 99(4), 625-
610 632.

611 Seidel, D. (1981) Extracting uranium from its ores. *IAEA Bulletin*, 23(2), 24-28.

612 Sharifironizi, M., Szymanowski, J.E., Sigmon, G.E., Navrotsky, A., Fein, J.B., and Burns, P.C.
613 (2016) Thermodynamic studies of zippeite, a uranyl sulfate common in mine wastes.
614 *Chemical Geology*, 447, 54-58.

615 Smith, P.A., Spano, T.L., and Burns, P.C. (2018) Synthesis and structural characterization of a
616 series of uranyl-betaine coordination complexes. *Zeitschrift für Kristallographie-
617 Crystalline Materials*, 233(7), 507-513.

618 Spano, T.L., Olds, T.A., McDonnell, M., Smith, R., Niedziela, J.L., Miskowicz, A., Kapsimalis,
619 R., and Shields, A.E. (2023) CURIES: Compendium of Uranium Raman and Infrared
620 Experimental Spectra. *American Mineralogist*, In Press.

621 Tyumentseva, O.S., Korniyakov, I.V., Britvin, S.N., Zolotarev, A.A., and Gurzhiy, V.V. (2019)
622 Crystallographic insights into uranyl sulfate minerals formation: Synthesis and crystal
623 structures of three novel cesium uranyl sulfates. *Crystals*, 9(12), 660.

624

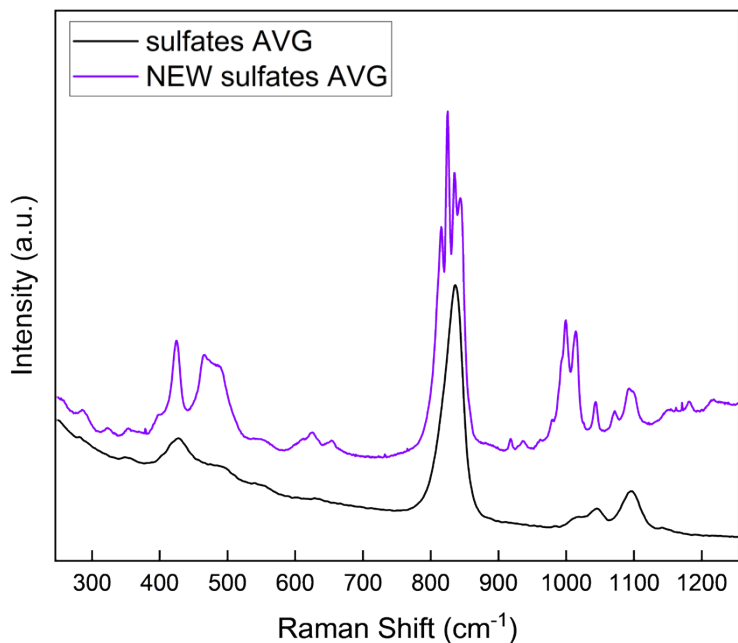
625

626

627

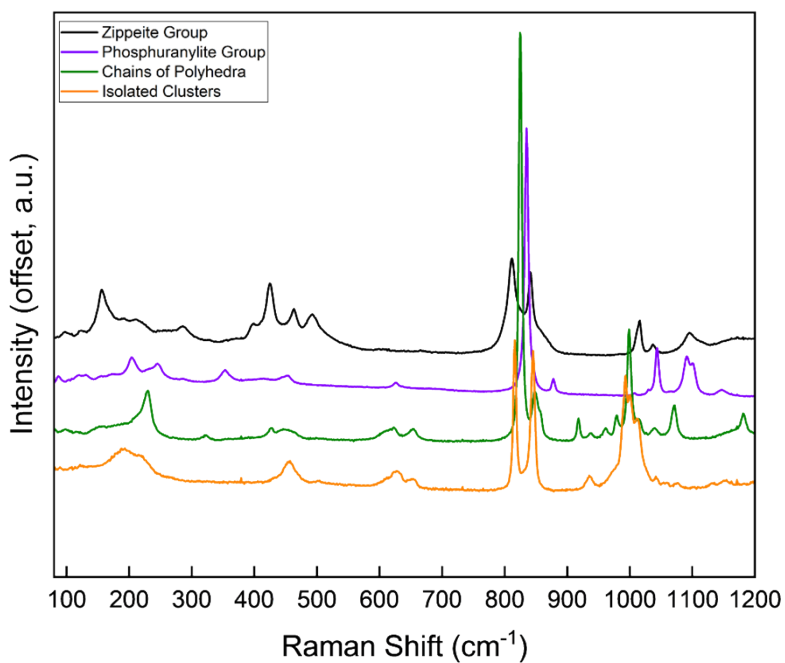
628

629



631

632 *Figure 1. Average uranyl sulfate spectra before (black) and after (purple) addition of Raman*
633 *spectra from this work.*



634

635 *Figure 2. Average spectra (offset) for groups of uranyl sulfate minerals based upon structure*
636 *type.*

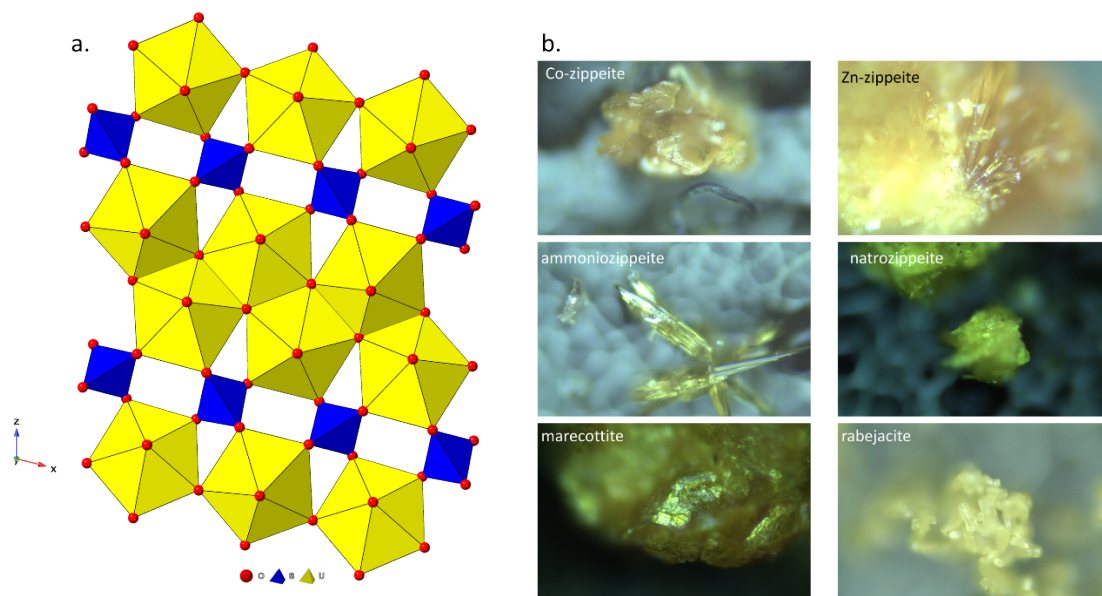
Table 1. Uranyl sulfate minerals included in this work.

Mineral Name	Structural Unit Type	Anion Topology	Ideal Formula	Space Group	Locality	Sample Description	Reference
Co-rich zippeite	sheet	zippeite	$\text{Co}(\text{UO}_2)_2(\text{SO}_4)\text{O}_2 \cdot 3.5\text{H}_2\text{O}$	<i>C2/m</i>	Blue Lizard mine, Red Canyon, UT	Flat orange prisms to ~10 μm	Burns, P. C. et al. 2003
Zn-rich zippeite	sheet	zippeite	$\text{Zn}(\text{UO}_2)_2(\text{SO}_4)\text{O}_2 \cdot 3.5\text{H}_2\text{O}$	<i>C2/m</i>	Burro mine, CO	Platy orange crystalline aggregates	Burns, P. C. et al. 2003
uranopilite	chain	dense chains of polyhedra	$(\text{UO}_2)_6(\text{SO}_4)\text{O}_2(\text{OH})_6 \cdot 14\text{H}_2\text{O}$	<i>P-1</i>	Burro mine, CO	Yellow prisms	Burns, P. C. et al. 2001
ammoniozippeite	sheet	zippeite	$(\text{NH}_4)_2[(\text{UO}_2)_2(\text{SO}_4)\text{O}_2] \cdot \text{H}_2\text{O}$	<i>P4/n</i>	Burro mine, CO	Thin, flat yellow spear-like crystals	Kampf, A. R. et al. 2018
ammoniomathiesiusite	sheet	mathiesiusite	$(\text{NH}_4)_5(\text{UO}_2)_4(\text{SO}_4)_4(\text{VO}_3) \cdot 4\text{H}_2\text{O}$	<i>P4/n</i>	Burro mine, CO	Yellow-green prisms and powdery aggregates	Kampf, A. R. et al. 2019
natrozippeite	sheet	zippeite	$\text{Na}_5(\text{UO}_2)_8(\text{SO}_4)_4\text{O}_5(\text{OH})_3 \cdot 12\text{H}_2\text{O}$	<i>P2_1/n</i>	A: Blue Lizard mine; B: Blue Lizard mine; C: Blue Lizard mine; D: Markey mine, UT; E: Burro mine	A: Yellow blades; B: yellow blades; C: small yellow blades; D: powdery masses; E: powdery masses	Burns, P. C. et al. 2003
johannite	sheet	phosphuranylite	$\text{Cu}(\text{UO}_2)_2(\text{SO}_4)_2(\text{OH})_2 \cdot 8\text{H}_2\text{O}$	<i>P-1</i>	Markey mine, UT	Pale green prisms	Hurlbut, C. S. 1950
marecottite	sheet	zippeite	$\text{Mg}_3(\text{UO}_2)_8(\text{SO}_4)_4\text{O}_6(\text{OH})_2 \cdot 28\text{H}_2\text{O}$	<i>P-1</i>	Blue Lizard mine, UT	Orange finely crystalline masses	Brugger, J. et al. 2003
lussierite	clusters	isolated clusters	$\text{Na}_{10}[(\text{UO}_2)(\text{SO}_4)_4](\text{SO}_4)_2 \cdot 3\text{H}_2\text{O}$	<i>Cc</i>	Blue Lizard mine, UT	Small green prisms	Kampf A. R. et al. 2003
zincrietveldite	sheets	chains of polyhedra	$\text{Zn}(\text{UO}_2)(\text{SO}_4)_2(\text{H}_2\text{O})_5$	<i>Pmn2_1</i>	Giveaway-Simplot mine, UT	Small yellowish-green blades	Kampf A. R. et al. 2022
navrotskyite	chains	chains of polyhedra	$\text{K}_2\text{Na}_{10}(\text{UO}_2)_3(\text{SO}_4)_9 \cdot 2\text{H}_2\text{O}$	<i>Pbcm</i>	Blue Lizard mine, UT	Thin, pale-green blades	Olds, T. A. et al. 2019
fermiite	chains	chains of polyhedra	$\text{Na}_4(\text{UO}_2)(\text{SO}_4)_5 \cdot 3\text{H}_2\text{O}$	<i>Pmn2_1</i>	Blue Lizard mine, UT	Aggregate of pale green platy crystals	Kampf, A. R., et al. 2015
belakovskiite	clusters	isolated clusters	$\text{Na}_7(\text{UO}_2)(\text{SO}_4)_4(\text{SO}_3\text{OH})(\text{H}_2\text{O})_3$	<i>P-1</i>	Blue Lizard mine, UT	Finely fibrous pale-green needles on gypsum	Kampf, A. R., et al. 2014
plásilite	sheet	phosphuranylite	$\text{Na}(\text{UO}_2)(\text{SO}_4)(\text{OH}) \cdot 2\text{H}_2\text{O}$	<i>P2_1/c</i>	Blue Lizard mine, UT	Thin green prisms	Kampf, A. R., et al. 2015
feynmanite	sheet	phosphuranylite	$\text{Na}(\text{UO}_2)(\text{SO}_4)(\text{OH}) \cdot 3.5\text{H}_2\text{O}$	<i>P2/n</i>	Markey mine, UT	Thin pale-green prisms	Kampf, A. R., et al. 2019
bluelizardite	isolated clusters	isolated clusters	$\text{Na}_7(\text{UO}_2)(\text{SO}_4)_4\text{Cl} \cdot \text{H}_2\text{O}$	<i>C2/c</i>	Blue Lizard mine, UT	Thin, stubby green prisms	Plásil, J., et al. 2014
meisserite	chains	chains of polyhedra	$\text{Na}_5(\text{UO}_2)(\text{SO}_4)_5(\text{SO}_3\text{OH})(\text{H}_2\text{O})$	<i>P-1</i>	Blue Lizard mine, UT	Anhedral green masses on gypsum	Plásil, J., et al. 2013
rabeiacite	sheet	zippeite	$\text{Ca}(\text{UO}_2)_x(\text{SO}_4)_y(\text{OH})_z \cdot 6\text{H}_2\text{O}$	<i>P-1</i>	Blue Lizard mine, UT	Small yellow plates	Plásil, J., et al. 2018

638 *Table 2. Assignment of features in the average Raman spectra for uranyl sulfate mineral groups*

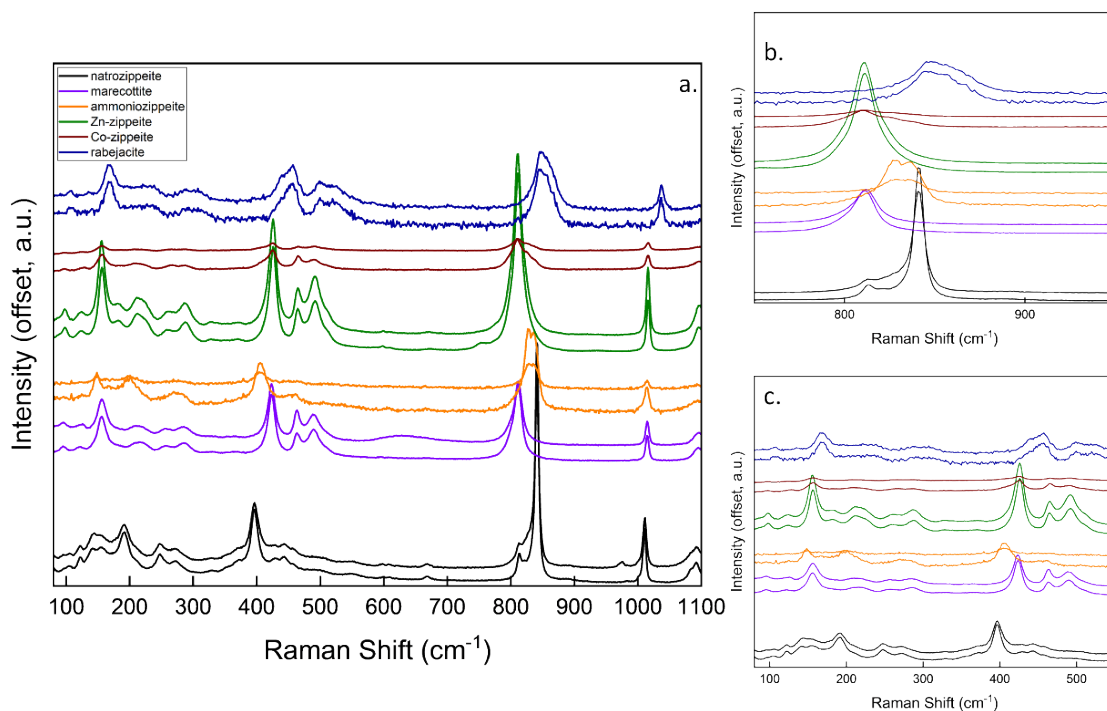
Feature (cm ⁻¹)	Structure Type	Assignment	Reference
157	zippeite	U-O equatorial modes	Plášil et al., 2010
~380-550	zippeite	$\nu_2\text{UO}_2^{2+}$, $\nu_3\text{SO}_4^{2-}$, U-O equatorial modes	Plášil et al., 2010; Frost et al., 2005a
810, 840	zippeite	$\nu_1\text{UO}_2^{2+}$	Plášil et al., 2010; Frost et al., 2005a
1015	zippeite	$\nu_1\text{SO}_4^{2-}$	Plášil et al., 2010
1095	zippeite	$\nu_3\text{SO}_4^{2-}$	Plášil et al., 2010
~190-260	phosphuranylite	$\nu_2\text{UO}_2^{2+}$	Kampf et al., 2019a; Frost et al., 2005b
350	phosphuranylite	U-O equatorial modes, or O-M [§] interactions	Kampf et al., 2019a; Kampf et al., 2018a
450	phosphuranylite	$\nu_2\text{SO}_4^{2-}$	Kampf et al., 2019a; Kampf et al., 2018a
625	phosphuranylite	$\nu_4\text{SO}_4^{2-}$	Kampf et al., 2019a; Kampf et al., 2018a
834, 875	phosphuranylite	$\nu_1\text{UO}_2^{2+}$	Frankland et al., 2022
1045-1115	phosphuranylite	$\nu_1\text{SO}_4^{2-}$, $\nu_3\text{SO}_4^{2-}$	Frankland et al., 2022; Frost et al., 2005b
230	chains of polyhedra	$\nu_2\text{UO}_2^{2+}$	Kampf et al., 2015b
~405-480	chains of polyhedra	$\nu_2\text{SO}_4^{2-}$	Kampf et al., 2015b; Kampf et al., 2017; Plášil et al., 2013a
~580-675	chains of polyhedra	$\nu_4\text{SO}_4^{2-}$	Kampf et al., 2015b; Kampf et al., 2017; Plášil et al., 2013a
824, ~840-860	chains of polyhedra	$\nu_1\text{UO}_2^{2+}$	Kampf et al., 2015b; Kampf et al., 2017; Plášil et al., 2013a
~900-1085	chains of polyhedra	$\nu_3\text{SO}_4^{2-}$	Kampf et al., 2015b; Kampf et al., 2017; Plášil et al., 2013a
~150-250	isolated clusters	$\nu_2\text{UO}_2^{2+}$	Kampf et al., 2019b
455	isolated clusters	$\nu_2\text{SO}_4^{2-}$	Kampf et al., 2019b
~595-670	isolated clusters	$\nu_4\text{SO}_4^{2-}$	Plášil et al., 2014b; Kampf et al., 2019b, Kampf et al., 2014
815, 845	isolated clusters	$\nu_1\text{UO}_2^{2+}$	Plášil et al., 2014b; Kampf et al., 2019b, Kampf et al., 2014
935, ~950-1080	isolated clusters	$\nu_1, \nu_3\text{SO}_4^{2-}$	Plášil et al., 2014b; Kampf et al., 2019b

[§]M = charge balancing species



640

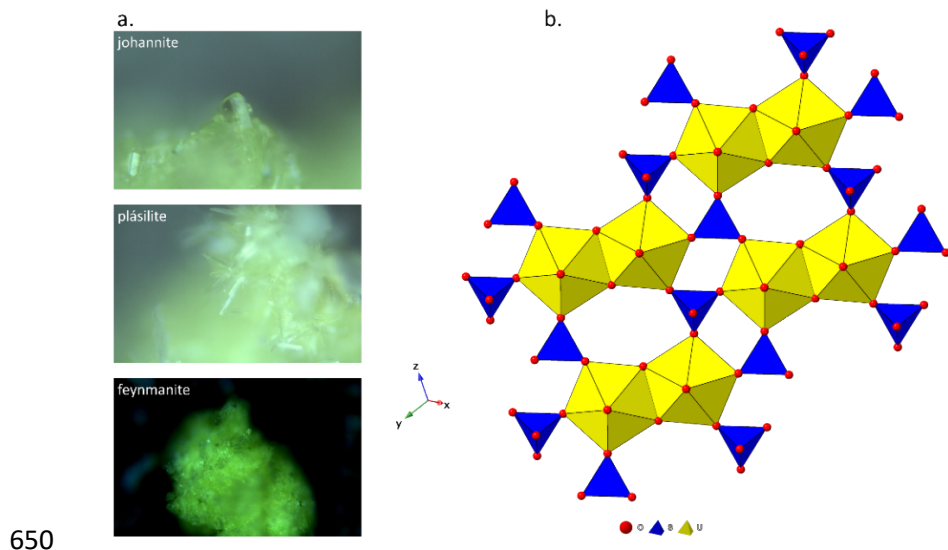
641 *Figure 3. a. The structural unit of minerals possessing the zippeite anion topology. b. Zippeite*
 642 *group minerals investigated in this work. Horizontal field of view for all sample photographs is*
 643 *450 μm .*



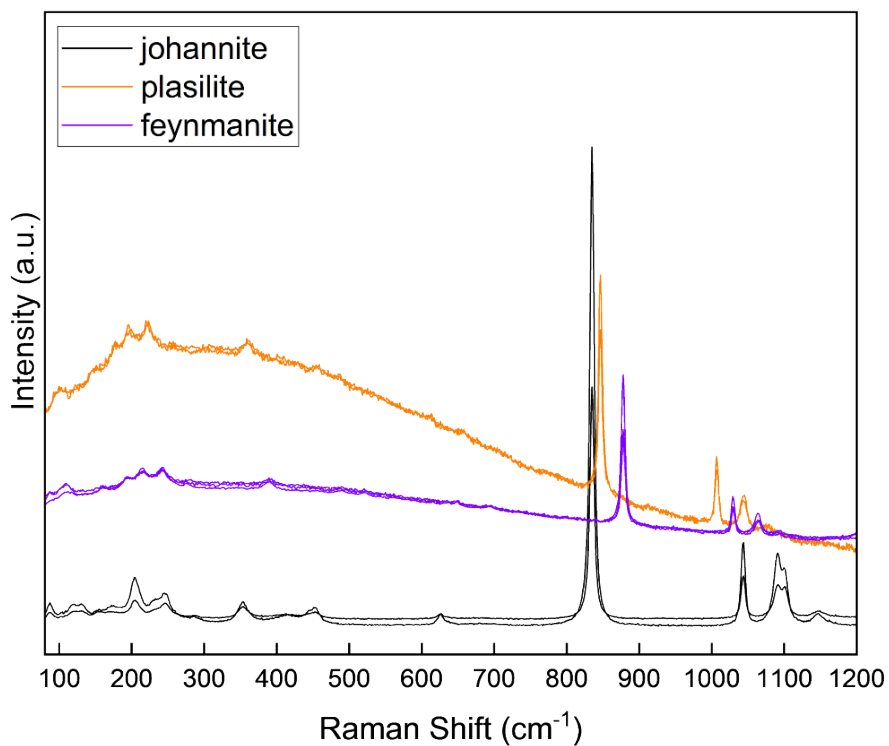
644

645 *Figure 4.a. Spectra (offset) for several uranyl sulfate minerals that possess the zippeite anion*
 646 *topology. For simplicity, two datasets are shown for each species and additional datasets*
 647 *collected for zippeite group minerals are included in Supporting Information. b. The uranyl*

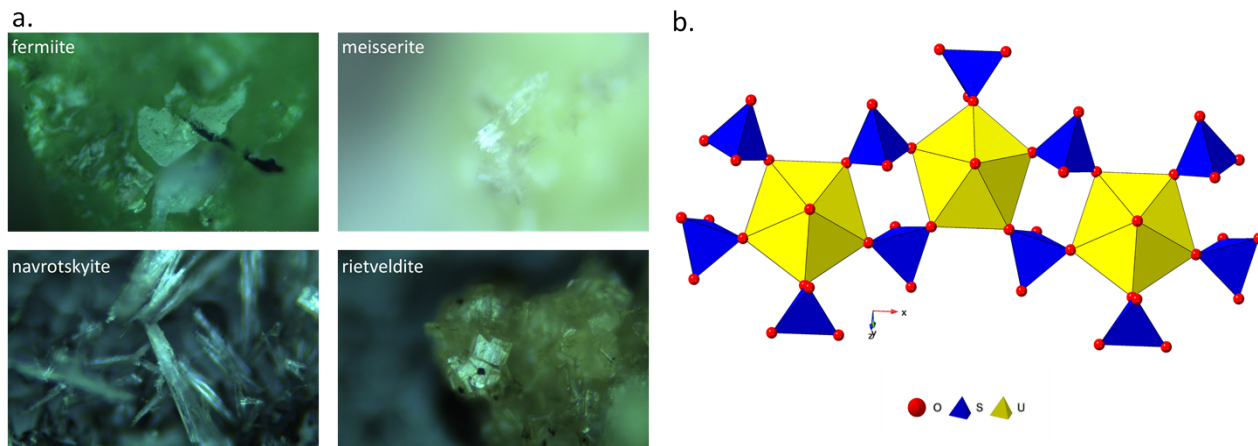
648 region of zippeite group uranyl sulfate spectra (offset). c. The low energy region of zippeite
649 group uranyl sulfate spectra (offset).



651 Figure 5. a. Phosphuranylite group minerals investigated in this work. Horizontal field of view
652 for all sample photographs is 450 μm . b. The phosphuranylite anion topology as seen in
653 johannite.



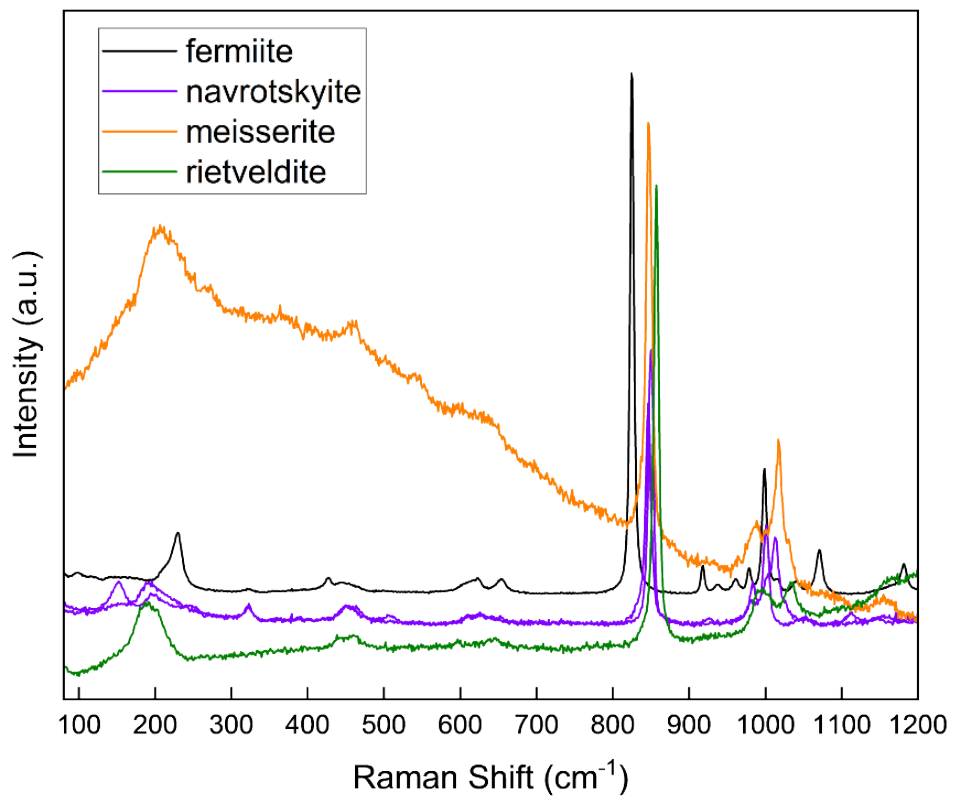
654
655 Figure 6. Spectra for uranyl sulfate minerals that possess the phosphuranylite anion topology.



656

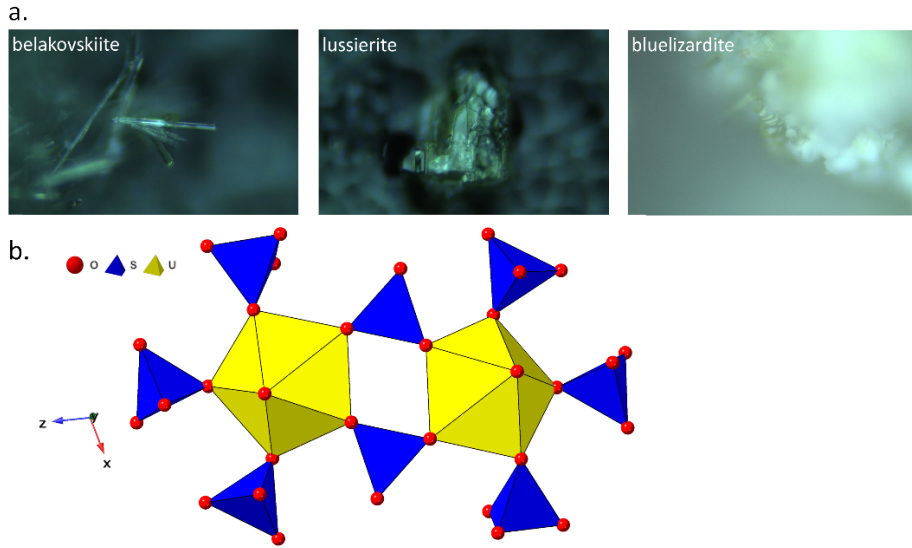
657 *Figure 7 a. Uranyl sulfate minerals investigated in this work that contain chains of polyhedra,*
 658 *such as fermiite (b). Horizontal field of view for all sample photographs is 450 μm .*

659



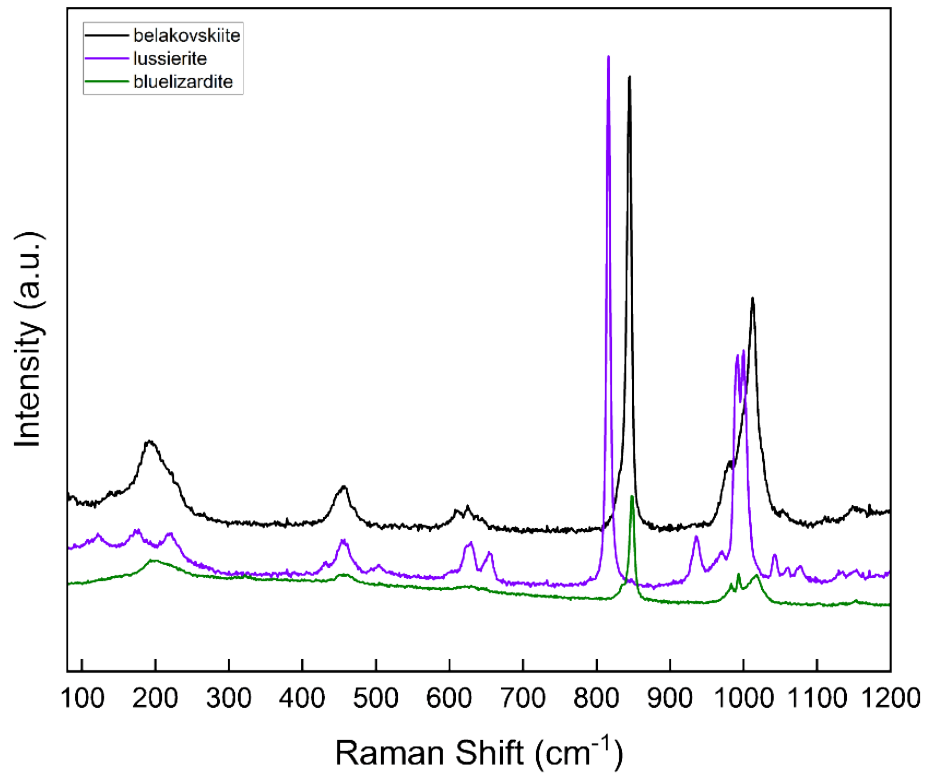
660

661 *Figure 8. Raman spectra collected for uranyl sulfate minerals composed of chains of polyhedra.*



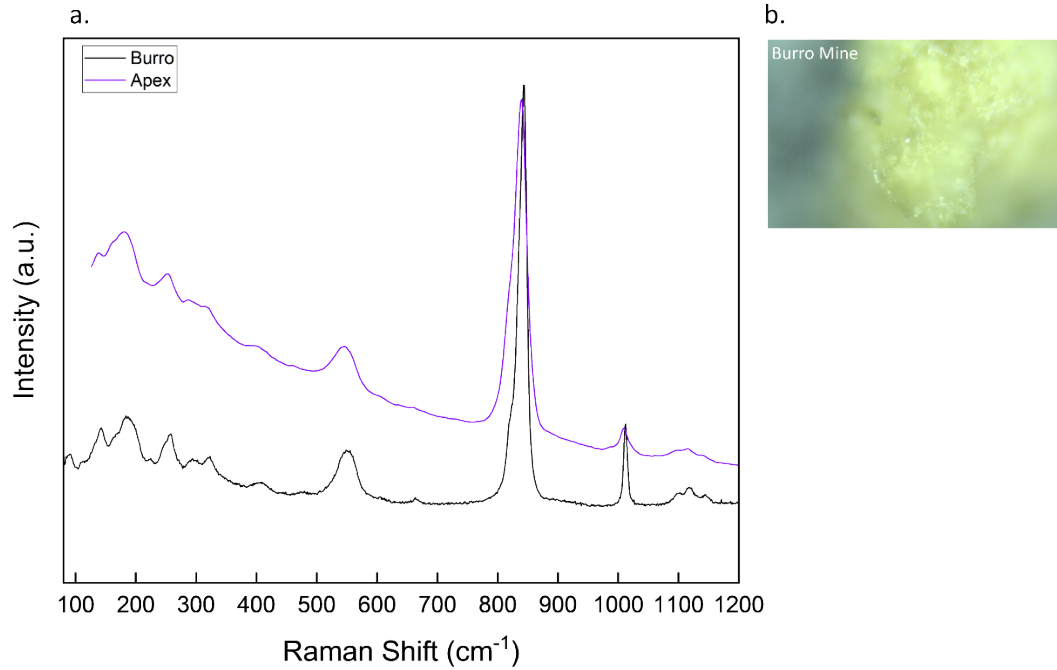
662

663 *Figure 9. a. Uranyl sulfate minerals composed of isolated clusters such as bluelizardite (b.).*
 664 *Horizontal field of view for all sample photographs is 450 μm .*



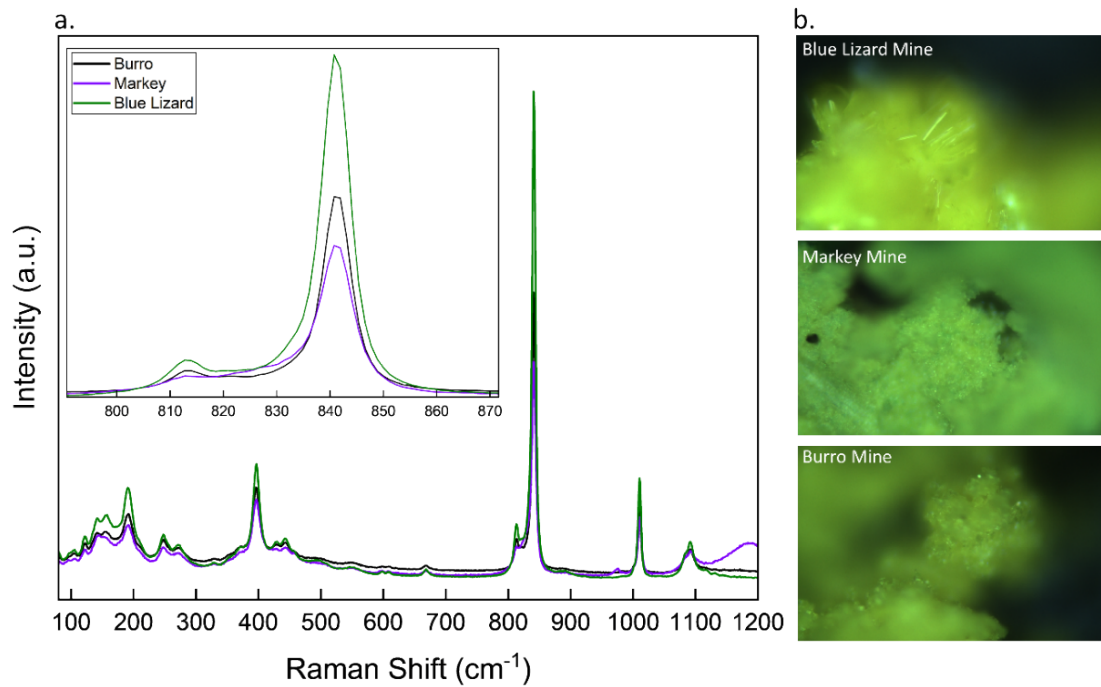
665

666 *Figure 10. Raman spectra collected for uranyl sulfate minerals composed of isolated clusters.*



667

668 *Figure 11. a. Comparison of Raman spectra collected for uranopilite (b.) in this work, and*
 669 *published data. Horizontal field of view for all sample photographs is 450 μm .*

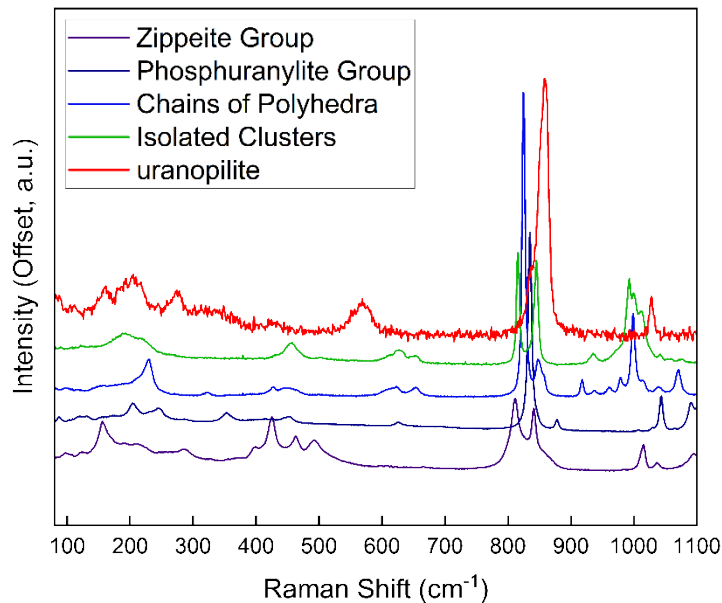


670

671 *Figure 12 a. Comparison of Raman spectra collected for natrozippeite (b.) for several localities.*
 672 *Horizontal field of view for all sample photographs is 450 μm .*

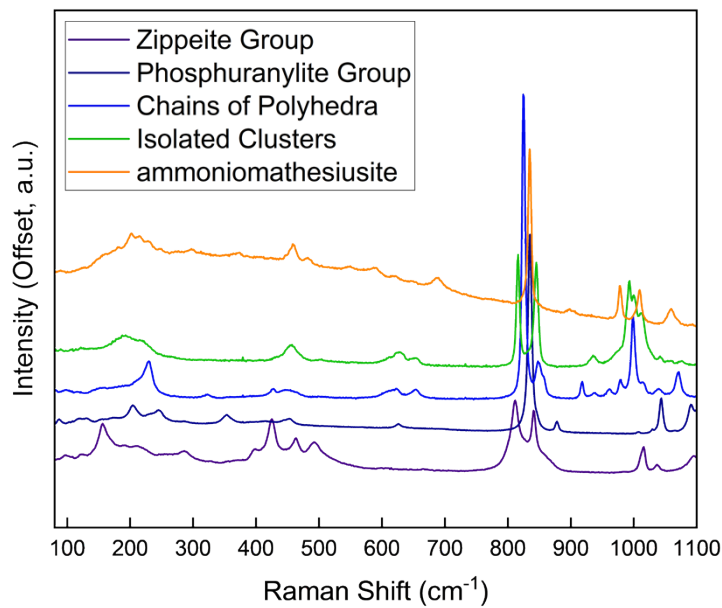
673 **Supporting Information**

674 **Figure S1.** Raman spectra for uranopilite compared with average spectra for other groups of
675 uranyl sulfate minerals.



676

677 **Figure S2.** Raman spectra for ammoniomathesiusite compared with average spectra for other
678 groups of uranyl sulfate minerals.



679